J. Mech. Phys. Solids 170 (2023) 105115

Contents lists available at ScienceDirect

Journal of the Mechanics and Physics of Solids

journal homepage: www.elsevier.com/locate/jmps

Fracture initiated from corners in brittle soft materials

Jason Steck [1], Sammy Hassan [1], Zhigang Suo [*]

John A. Paulson School of Engineering and Applied Science, Harvard University, 29 Oxford Street, Pierce 309, Cambridge, MA 02138, USA

ARTICLE INFO

Keywords:
Corner
Fracture
Singularity
Finite deformation
Lap shear

ABSTRACT

This paper studies a commonly observed phenomenon: the initiation of fracture from corners in a brittle soft material. A rectangular hydrogel is prepared and glued between two plastic films, such that the hydrogel meets the films at 90° corners. When the two plastic films are pulled, the hydrogel undergoes a shear deformation, and the stress-strain curve is recorded until fracture initiates from a corner. We find that the shear modulus is independent of the thickness H of the hydrogel, but the shear strength scales as $\sim H^{-0.4}$. A numerical simulation shows a nonlinear elastic zone around the corner, in which the stress field varies slowly. However, when the nonlinear elastic zone is small compared to the thickness, an annulus exists in which a singular field of linear elasticity prevails. In this annulus, the stress field scales with the distance R from the corner as $\sim R^{-0.41}$. We call this condition small-scale nonlinear elasticity. Our results indicate that small-scale nonlinear elasticity prevails even when the applied shear strain is as large as 80%. This condition explains the experimentally observed scaling between strength and thickness. The condition of small-scale nonlinear elasticity simplifies the characterization of fracture initiated from corners of brittle soft materials.

1. Introduction

Corners concentrate stress and often initiate fracture. For hard materials, the stress around a corner intensifies by a singular field of linear elasticity (Williams, 1952; Bogy, 1971; Hein and Erdogan, 1971). The exponent of the singularity m depends on the angle of the corner and elastic mismatch between the materials. This linear elastic singularity is used to correlate the experimental conditions under which fracture initiates from corners in hard materials of various shapes and sizes (Reedy, 1990; Reedy and Guess, 1993; Liu and Fleck, 1999; Dunn et al., 2000; Labossiere and L. Dunn, 2001). In particular, the strength is found to scale with the length scale L of the experiment as $\sim L^{-m}$.

Even though fracture in nonlinear elastic materials also often initiates from corners, it is unknown whether a similar approach to that described above can be applied. This question is studied in the present paper. We prepare a rectangular polyacrylamide hydrogel and glue it between two inextensible polyester films. The edges of the hydrogel meet the films to form 90-degree corners. The hydrogel is lap-sheared until fracture initiates from a corner. We record the shear stress-strain curves for hydrogels of different thicknesses H. Whereas the shear modulus is independent of H, the shear strength scales as $\sim H^{-0.4}$ (Section 2). We then simulate the lap shear test with finite elements. A nonlinear elastic zone exists around the corner, in which the stress field varies slowly. When the nonlinear elastic zone is small compared to the thickness of the hydrogel, an annulus exists in which a singular field of linear elasticity prevails.

* Corresponding author.
E-mail address: suo@seas.harvard.edu (Z. Suo).
[1] These authors contributed equally to this work.

https://doi.org/10.1016/j.jmps.2022.105115
Received 10 August 2022; Received in revised form 17 October 2022; Accepted 17 October 2022
Available online 22 October 2022

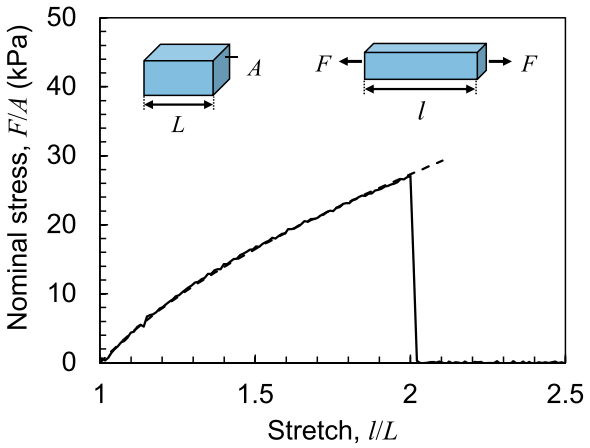

Fig. 1. Uniaxial stress-stretch curve. Define the nominal stress by dividing the tensile force by the cross sectional area of the undeformed sample, F/A. Define the stretch by dividing the deformed length by the undeformed length, l/L. The dashed line is the neo-Hookean model with a shear modulus of $\mu = 15.6$ kPa.

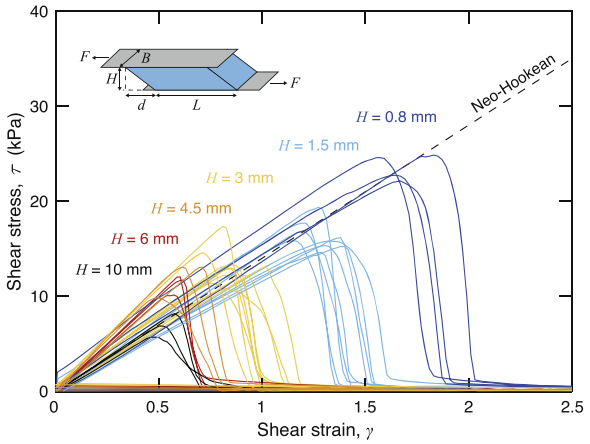

Fig. 2. Shear stress-strain curves of samples of various thicknesses obtained by lap shear. For each thickness, multiple samples are tested. Define the shear stress by $\tau = F/BL$ and the shear strain by $\gamma = d/H$. A neo-Hookean stress-strain curve is plotted with a shear modulus of $\mu = 14$ kPa.

Inside the annulus, the stress field closely matches that of linear elasticity–that is, the stress field scales with the distance R from the corner as $\sim R^{-0.41}$ (Section 3). We call this condition small-scale nonlinear elasticity. Our numerical simulation shows that the small-scale nonlinear elasticity condition holds when the hydrogel fractures at a shear strain as large as 80%. We interpret the experimentally observed strength-thickness scaling in terms of the linear elastic singular field (Section 4). We calculate the corner toughness from the experimental results and show that it is independent of thickness. The condition of small-scale nonlinear elasticity simplifies the characterization of fracture initiated from corners of brittle soft materials.

2. Lap shear of a soft material

2.1. Sample preparation

We prepare polyacrylamide (PAAm) hydrogels by free radical polymerization of acrylamide monomer (Sigma Aldrich, A8887), using N,N'-methylenebisacrylamide crosslinker (Sigma Aldrich, M7279) and 2-hydroxy-4′(2-hydroxyethoxy)-2-methylpropiophenone photoinitiator (Sigma Aldrich, 410896). The molar ratios of water, crosslinker, and initiator to monomer are 25, 5×10^{-3}, and 5×10^{-4}, respectively. The resulting hydrogels are 86 wt% water. We perform a uniaxial tensile test on the hydrogel, and find that the stress-stretch curve is well represented by the neo-Hookean model (Fig. 1).

Rectangular samples are cut from a large sheet of the hydrogel with a razor blade. A sample of the hydrogel is glued between two polyester films (McMaster-Carr, 8567K92) using cyanoacrylate (Krazy glue). The edges of the hydrogel meet the surfaces of the films to form 90-degree corners.

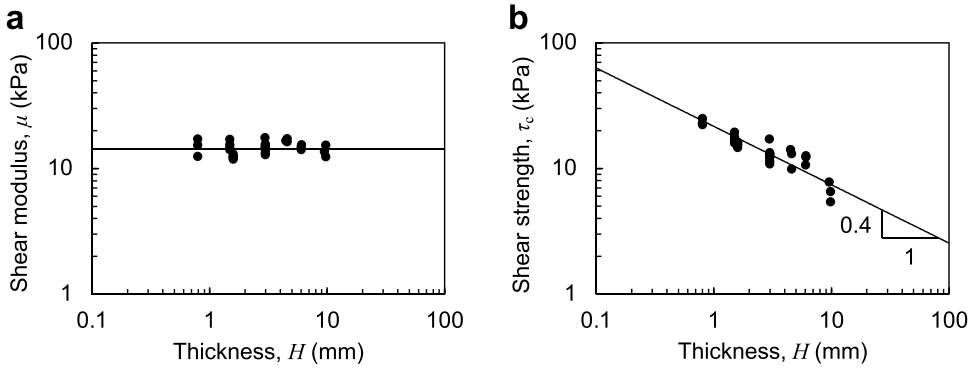

Fig. 3. Shear modulus and shear strength of the hydrogels of various thicknesses. (a) Shear modulus is independent of thickness. (b) Shear strength scales with the thickness as $\tau_c \sim H^{-0.4}$.

2.2. Lap shear

Lap shear is commonly used to characterize soft layers (Banea and da Silva, 2009; da Silva et al., 2009a, 2009b). Here we lap shear a PAAm hydrogel bonded between two polyester films (Fig. 2). Define the shear stress τ and shear strain γ by

$$\tau = F/BL, \gamma = d/H \tag{1}$$

where F is the force applied to the polyester films, d is the relative displacement of the two films, and H, B and L are the thickness, width, and length of the hydrogel, respectively. The width B is chosen to be much larger than the thickness H, such that the hydrogel deforms under the plane strain conditions.

The stress and strain defined by Eq. (1) call for some explanation, because lap shear deforms the hydrogel inhomogeneously. The corners concentrate stress, but the regions of stress concentration are small compared to the length L of the hydrogel if $L/H >> 1$. However, when the length L is too long, the shear lag effect will remove shear stress in the middle portion of the hydrogel (Cox, 1952; Hui et al., 2018; Wang et al., 2020). The shear lag model identifies a length scale:

$$L_s = (E_b H_b H/\mu)^{1/2}, \tag{2}$$

where E_b and H_b are the Young's modulus and thickness of the stiff layers and μ is the shear modulus of the soft layer. When $H << L << L_s$ a large portion of the hydrogel deforms by nearly homogeneous shear. In our experiments, we choose L such that this condition holds. Taking $H = 1$ mm, $\mu = 14$ kPa, $H_b = 0.25$ mm, and $E_b = 3$ GPa, we estimate $L_s \sim 23$ cm. As a result, the polyester films behave like inextensible tapes. The shear stress-strain curve prior to fracture is governed by the average deformation over the entire sample, whereas the fracture condition is governed by the stress concentration at the corners. Consequently, lap shear allows us to obtain reliable stress-strain curves up until fracture.

Hydrogels have time-dependent rheological behavior. Leading effects include viscoelasticity and poroelasticity. Our experiments are conducted in dry air, and the applied shear strain rate is held constant at $0.2\ s^{-1}$. The applied shear strain at rupture is between 0.5 and 2, giving a time to rupture on the order of ~10 s. Viscoelasticity of the polyacrylamide hydrogel has been studied by measuring hysteresis in the stress-stretch curves, and the stretch-rate effect on the stress-stretch curves (Hassan et al., 2022; Kim et al., 2021). Both types of experiment have shown that the polyacrylamide hydrogel has negligible viscoelasticity. The length scale associated with poroelasticity is estimated as $L \sim (Dt)^{0.5}$, where t is the time scale of the experiment and D is the diffusion coefficient of water (Hong et al., 2008). Taking $t \sim 10$ s and $D \sim 10^{-10}\ m\ s^{-2}$, we estimate $L \sim 10^{-6}$ m, beyond which the material is elastic within the time of the experiment. The length scale L is much smaller than the thickness of the hydrogel $H \sim 1$ mm, so through-thickness migration of water in the hydrogel is negligible. This length scale L is comparable to the size of the fracture process zone in polyacrylamide hydrogels (Chen et al., 2017), so that migration of water is contained within the fracture process zone. In this paper, we treat the hydrogel outside of the fracture process zone as a neo-Hookean elastic solid. There are no studies on the effect of poroelasticity on the initiation of fracture near corners, but there are studies of this effect on crack growth (Bouklas et al., 2015; Garyfallogiannis et al., 2022; Noselli et al., 2016; Wang and Hong, 2012). Ample opportunity exists to study the effect of poroelasticity on the initiation of fracture near corners and crack growth in hydrogels.

2.3. Shear stress-strain curves

We measure the shear stress-strain curves for hydrogels of thicknesses H (Fig. 2). Prior to fracture, the stress-strain curves are linear for all thicknesses. For each shear stress-strain curve, the slope defines the shear modulus μ, and the maximum stress defines the shear strength τ_c. For a neo-Hookean material under shear deformation, the stress-strain relation is linear for strain of any magnitude (Wang et al., 2020):

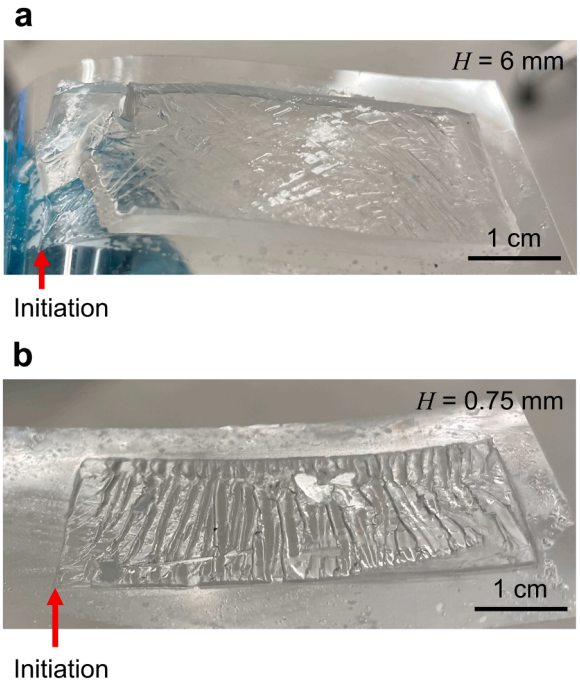

Fig. 4. Morphology of fracture. After initiating at a corner, a crack grows in the hydrogel. (a) For a thick hydrogel, $H = 6$ mm, the crack follows the interface for some distance before kinking to the other film, and then grows along the other interface. (b) For a thin hydrogel, $H = 0.75$ mm, the crack kinks periodically between the two films.

$$\tau = \mu\gamma. \tag{3}$$

Both the moduli and the strengths vary from sample to sample. The moduli show no systematic dependence on thickness, but the strengths show clear dependence on thickness. These observations are also evident when modulus and strength are plotted as functions of thickness (Fig. 3). The average shear modulus is $\mu = 14$ kPa. The shear strength scales with thickness as $\tau_c \sim H^{-0.4}$. The remainder of the paper sets out to understand these trends.

In each run of the experiment, fracture initiates from a corner of the hydrogel, near the interface between the hydrogel and a polyester film (Fig. 4). Fracture initiates when the shear stress-strain curve peaks. After fracture initiates, the stress drops precipitously, and a crack grows unstably until it reaches the other end of the hydrogel. When the hydrogel is thick, the crack grows near the interface for some distance, kinks to the other interface, and then grows near the interface until it reaches the other end of the hydrogel (Fig. 4a). When the hydrogel is thin, the crack kinks periodically between the two interfaces (Fig. 4b). This periodic crack trajectory looks similar to that observed in a thin epoxy layer between two aluminum substrates (Chai, 1986). Note that the epoxy layer is loaded by a double-cantilever beam, but the hydrogel is loaded by lap shear. It is unclear to us whether the periodic crack trajectories in the two materials are coincidental. Since this work focuses on fracture initiation, we will not study the crack trajectories further. In all cases, even when the crack grows near an interface, fracture is cohesive. There are always thin layers of hydrogel left on the polyester films.

We now consider whether fracture at the corner is governed by the presence of unintentional flaws. We measure the fracture toughness, $G_c \sim 35$ J/m^2, by lap shear of the hydrogel containing a long precrack (Wang et al., 2020). We calculate the work of fracture, $W_c \sim 900$ J/m^3, by the area under the tensile stress-stretch curve of the hydrogel containing no precrack (Fig. 1). The ratio, G_c/W_c, defines a material specific length, called the fractocohesive length (Chen et al., 2017). The fractocohesive length of the hydrogel is $G_c/W_c \sim 40$ μm. Since the fractocohesive length is larger than the size of typical flaws created during sample preparation, it is unlikely that fracture is governed by unintentional flaws. Furthermore, since the statistical scatter is similar for the modulus and strength (Fig. 3), it is unlikely that there are significant flaws of unknown length causing fracture initiation. Therefore, we hypothesize that fracture initiation is governed by the stress concentration at the corner.

3. Stress field near a corner

3.1. Linear elasticity

Stress concentrates near a corner. In linear elasticity, the stress field is power-law singular (Williams, 1952; Bogy, 1971; Hein and Erdogan, 1971):

$$\sigma_{ij}(R, \Theta) = kR^{-m} f_{ij}(\Theta), \tag{4}$$

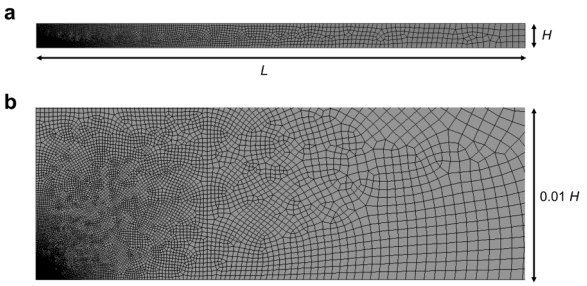

Fig. 5. Finite element model. (a) Mesh of an entire sample, length L and thickness H, sandwiched between two rigid substrates. When the top substrate is sheared relative to the bottom substrate by a displacement d, the sample deforms under the plane strain conditions. (b) Mesh near a corner in a region of height 0.01 H.

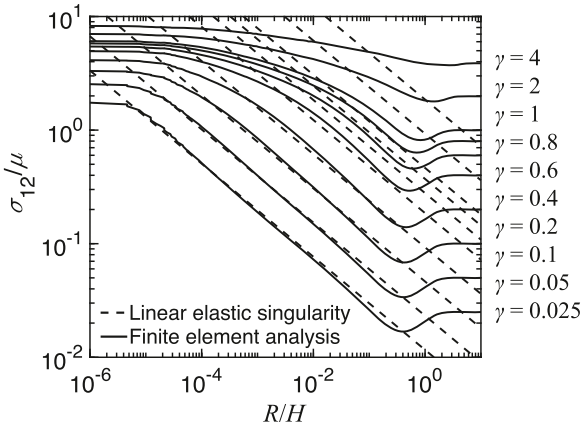

Fig. 6. Finite element results. Normalized true shear stress, σ_{12}/μ, as a function of R/H for different applied strains $\gamma = d/H$. The shear stress is evaluated along the boundary at $\Theta = 0$. The dashed lines are the linear elastic solution evaluated from Eq. (6) with $Y = 0.22$ for each γ.

where k is the loading parameter that scales the magnitude of the stress field, R is the radial distance from the corner, Θ is the radial angle, m is the power of the singular field, and $f_{ij}(\Theta)$ are the angular functions. The exponent m is determined by the geometry and the mechanical properties of the materials. For a soft material deforming under the plane strain conditions, bonded to a rigid material with a 90-degree corner, linear elasticity predicts that $m = 0.41$.

3.2. Nonlinear elasticity

The stress field in a nonlinear elastic material depends on the material model (Long and Hui, 2015). For an incompressible neo-Hookean material, the field around a corner does not have a published analytical solution. Results for a compressible material model are discussed in Appendix A, which complements several recently published works (Hui et al., 2022; Lengyel et al., 2014; Mo et al., 2021; Tarantino, 1999) . Here we use finite elements to simulate the nonlinear elastic field in lap shear. We model the hydrogel as a neo-Hookean solid using the commercial software ABAQUS. A hydrogel of length $L = 100$ mm and thickness $H = 5$ mm is subject to a prescribed displacement d on the top boundary (Fig. 5a). The displacement of the bottom boundary is set to zero. The left and right boundaries are traction free. The hydrogel is taken to be incompressible, a condition that we approximate by setting Poisson's ratio to 0.495. We use plane strain hybrid quadrilateral and triangular elements throughout the entire model. To resolve the corner stress concentration, we use a refined mesh near the bottom-left corner (Fig. 5b). A polar coordinate system in the undeformed state (R, Θ) is centered at the bottom-left corner. Near this corner, the mesh becomes 10 times finer for every decade in R, producing a logarithmic mesh spacing in R. The minimum mesh size near the corner is $2 \times 10^{-6}\, H$.

The true stress σ_{12} at $\Theta = 0$ is plotted as a function of R for different applied strains (Fig. 6). The shear stress is normalized by the shear modulus. Since the thickness of the sample is much smaller than the length, the near-corner field is insensitive to the length L, and we normalize the radius by the thickness H. When the applied shear strain is $\gamma = 0.025$, the shear stress recovers the applied shear stress when $R > 2\, H$, and bends to a high level when $R < 10^{-5}\, H$. In an intermediate interval, $10^{-5}\, H < R < 3 \times 10^{-1}\, H$, the scaling of the shear stress approximately matches that of a linear elastic plane strain corner on a rigid substrate, where $\sigma_{12} \sim R^{-0.41}$ when Poisson's ratio is 0.5 (Williams, 1952; Reedy, 1990). When γ is between 0.025 and 0.8, the shear stress scales according to the linear elastic singularity for intermediate R/H, and varies slowly at small R/H. This slow variation of σ_{12} is consistent with the behavior of a nearly incompressible Blatz-Ko material near a corner, for which we show the true stress is not power-law singular (Appendix A). We

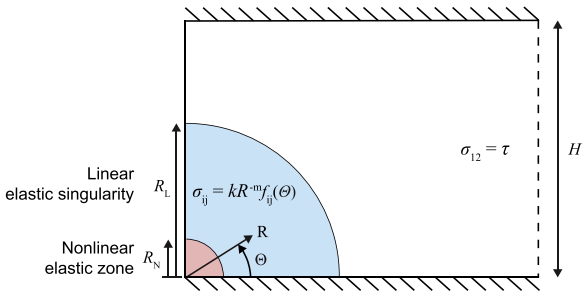

Fig. 7. Small-scale nonlinear elasticity. A polar coordinate system (R, Θ) is centered at a corner. Near the corner, a nonlinear elastic zone of size R_N exists. When $R_N << H$, an annulus of inner radius R_N and outer radius R_L exists, in which the linear elastic singularity prevails. Far from the corner, the material has uniform shear stress, τ.

designate the nonlinear elastic zone as the region of small R/H where the scaling of the shear stress deviates from the linear elastic singularity. For $\gamma = 1$, 2, and 4, the scaling of the shear stress does not match the linear elastic singularity for any R/H. We plot the remaining components of the stress field and the strain energy density, W, along $\Theta = 0$ in Appendix B (Fig. B1). The variation of σ_{11} and W with R/H closely follow that of σ_{12}. The true stresses σ_{22} and σ_{33} also follow the linear elastic singularity for intermediate R/H and γ, but plateau rapidly to μ for small R/H.

The stress field and strain energy density along $\Theta = 45$ are plotted as functions of R/H for different applied strains (Fig. B2). Both the stress field and the strain energy density along $\Theta = 45$ resemble those along $\Theta = 0$, following the scaling of the linear elastic singularity for intermediate values of R/H and γ. This suggests that the region where the stress field is described by a linear elastic singularity is annular, provided that $\gamma < 0.8$. Furthermore, the stress σ_{12} is plotted as a function of Θ with constant R/H and different applied strains (Fig. B3). We also plot the remaining components of the stress field along $R/H = 10^{-1}$ as functions of Θ (Fig. B4). All components fluctuate with Θ when the strain is small, but are approximately constant with Θ when the strain is large. The transition between the small and large strain behaviors occurs gradually between $\gamma = 0.1$ and $\gamma = 1$.

4. Small-scale nonlinear elasticity

The stress field near a corner of a linear elastic material is power-law singular, while that of a nonlinear elastic material is not (Section 3). However, a zone can exist in a nonlinear elastic material where the stress field is described by a linear elastic singularity, provided the deformation is small. Inside this zone, the stress increases while approaching the corner, until the material behaves nonlinearly. We denote the radius of this transition as R_N (Fig. 7), which scales the size of the nonlinear elastic zone. On the other hand, the linear elastic singularity does not describe the stress field near the boundaries of the sample, where it is instead set by the far field loading. We denote the upper radius for which the linear elastic singularity holds by R_L (Fig. 7), where R_L is much smaller than the length scale of the boundaries. In lap shear, this length scale is the thickness H. These two lengths, R_N and R_L, define an annulus in which a singular field of linear elasticity prevails. This region is called the k-annulus.

When R_N is smaller than R_L, the k-annulus exists. We call this condition small-scale nonlinear elasticity. This is analogous to the small-scale yielding condition (Anderson, 2017). When this condition holds, the stress field in the k-annulus is independent of the material behavior inside the nonlinear elastic zone. When the size of the nonlinear elastic zone is comparable to the size of the body, small-scale nonlinear elasticity does not hold, and the nonlinear boundary value problem must be solved. This is analogous to large-scale yielding in elastic-plastic fracture mechanics, where the solution of the HRR field is required to correlate the experiment conditions of fracture (Hutchinson, 1968; Rice and Rosengren, 1968).

Our finite element results indicate that the k-annulus exists when $\gamma < 0.8$ (Fig. 6). Therefore, we analyze the corner using the small-scale nonlinear elasticity condition and correlate the predictions with the experimental data in Fig. 3. We note that our analysis with the small-scale nonlinear elasticity condition is independent of the material behavior inside the nonlinear elastic zone.

4.1. Loading parameter k

We now connect the loading conditions to the linear elastic singularity. The applied shear strain γ produces a uniform shear stress $\tau = \mu\gamma$ in the bulk of the gel. τ is transmitted to the corner through the loading parameter k, producing the stress field $\sigma_{ij}(R, \Theta)$ in Eq. (4). k is the only parameter linking the far field loading to the singular stress field. Dimensional analysis and linearity require that k should take the form:

$$k = Y\tau H^m, \tag{5}$$

where Y is a function of the dimensionless parameters of the system. The variation of Y with L/H follows the same considerations as Eq. (1). When $H << L << L_s$ a large portion of the sample deforms homogeneously, and Y will not vary with L/H. Furthermore, we have assumed that the material is incompressible, so that the linear boundary value problem has no dimensionless parameter. Thus, Y is a dimensionless constant.

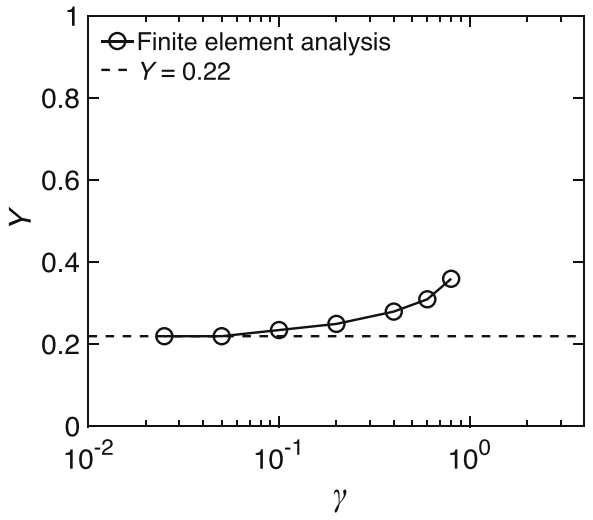

Fig. 8. The dimensionless function Y as a function of applied shear strain γ. The dashed line corresponds to $Y = 0.22$.

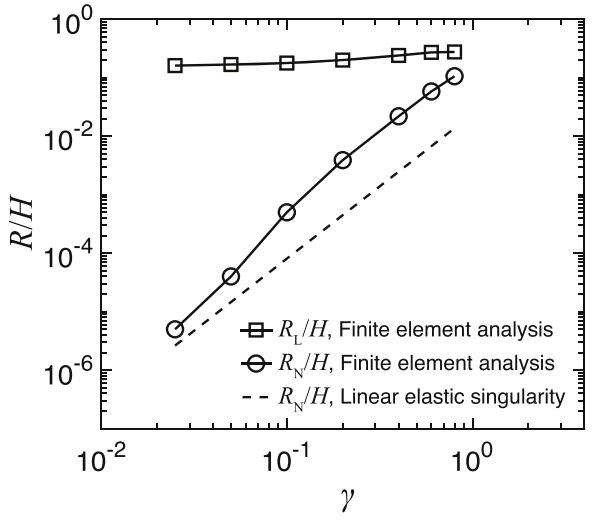

Fig. 9. The normalized linear elastic annulus size, R_L/H, and nonlinear elastic zone size, R_N/H, as functions of applied shear strain γ. The dashed line is the linear elastic scaling of R_N/H in Eq. (7).

We now write the singular stress field in terms of the far field strain, γ. Combining Eqs. (3), (4), and (5), and normalizing $f_{12}(\Theta)$ such that $f_{12}(\Theta) = 1$ at $\Theta = 0$ gives:

$$\sigma_{12}(R, \Theta = 0) = Y\mu\gamma(R/H)^{-m}. \tag{6}$$

We calibrate the parameter Y by matching Eq. (6) to the data in Fig. 6. Since Eq. (6) assumes linear elasticity, Y does not vary with the far field strain. Therefore, we evaluate Y at $\gamma = 0.025$ to be $Y = 0.22$. The linear results plotted in Fig. 6 correspond to Eq. (6) with $Y = 0.22$ for each γ. We note, however, that the deformation is not infinitesimal when γ is larger than a few percent. At large γ, finite deformation causes the linear elastic singularity to deviate from the finite element results in the k-annulus (Fig. 6). To quantify the magnitude of this effect, we plot Y as a function of γ in Fig. 8, where Y is calculated by matching Eq. (6) to the finite element results in the k-annulus for each γ. Y varies from $Y = 0.22$ for $\gamma < 0.1$ to $Y = 0.38$ at $\gamma = 0.8$. Since Y is a weak function of γ over multiple orders of magnitude, we expect the error from using $Y = 0.22$ to be small when correlating the predictions from this method with the experimental data.

Note that since the simulation was run with constant thickness, there can be a normal stress developed at the boundaries due to the Poynting effect (Truesdell and Noll, 2004). This effect is absent in linear elasticity, and is purely a result of finite deformation. We observe this effect in the true stress σ_{11} far from the corner (Fig. B1b). At $R/H = 10$, σ_{11} is negligible when γ is small, but of comparable magnitude to σ_{12} when $\gamma \sim 1$. It is possible that this stress can influence the stress field near the corner. However, the linear elastic

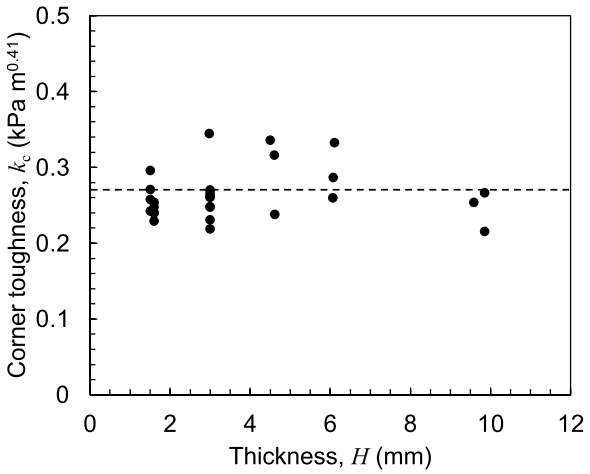

Fig. 10. Corner toughness k_c as a function of thickness. A horizontal line is drawn at the average corner toughness of 0.27 Pa m$^{0.41}$.

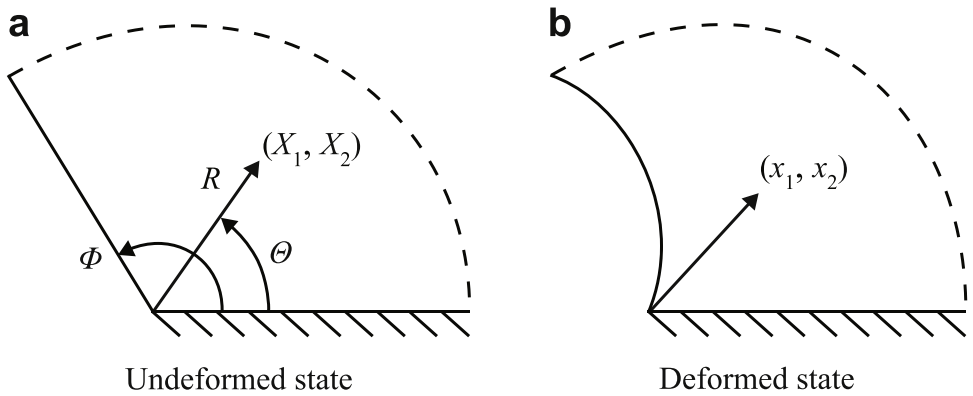

Fig. A1. Wedge of angle Φ undergoing finite plane strain deformation on a rigid substrate. Coordinate systems are centered at the intersection of the traction-free and displacement-free boundaries. A material particle is labeled by (a) (X_1, X_2) and (R, Θ) in the undeformed state and (b) (x_1, x_2) in the deformed state.

solution in Eq. (6) with $Y = 0.22$ accurately predicts σ_{12} in the linear elastic annulus up to $\gamma \sim 0.8$. Eq. (6) does not include the effects of normal stresses at the boundaries when $Y = 0.22$. Therefore, we do not consider how normal stresses at the boundaries affect the near-corner stress field in this paper. More research is needed into the relationship between the Poynting effect and the stress fields near corners and cracks.

4.2. Nonlinear elastic zone size

R_N and R_L are measured from the finite element results. Note that the linear elastic singularity is represented in Fig. 6 by lines of constant slope, equal to -0.41. By contrast, the slopes of the finite element results are approximately equal to -0.41 inside the *k*-annulus, but deviate from -0.41 outside the *k*-annulus. That is, for a given applied strain γ, the slope of the finite element result deviates from the linear elastic singularity twice. We define R_N and R_L, respectively, as the smaller and larger radii where the slope deviates from that of the linear elastic singularity by 10%. When the applied strain is very large, the slope deviates from -0.41 by greater than 10% for all R/H. In this case, the *k*-annulus does not exist, and R_N and R_L are not defined. We plot R_N/H and R_L/H as functions of γ in Fig. 9. R_N/H increases with γ, while R_L/H is approximately independent of γ at $R_L/H = 3 \times 10^{-1}$. When $R_N << R_L$, small-scale nonlinear elasticity holds. In Fig. 9, we see that small-scale nonlinear elasticity holds for γ up to 0.8.

In ductile metals, the size of the nonlinear zone is typically estimated by setting the shear stress in the singular field equal to the yield stress (Anderson, 2017). By contrast, a nonlinear elastic material behaves nonlinearly when the stress is on the order of the modulus (Long et al., 2021). Therefore, we estimate the size of the nonlinear elastic zone, R_N, by setting $\sigma_{12} \sim \mu$ in Eq. (6):

$$R_N \Big/ H \sim (\gamma Y)^{1/m} \tag{7}$$

We plot Eq. (7) as the dashed line in Fig. 9. The nonlinear elastic zone size is predicted from the linear elastic singularity up to a

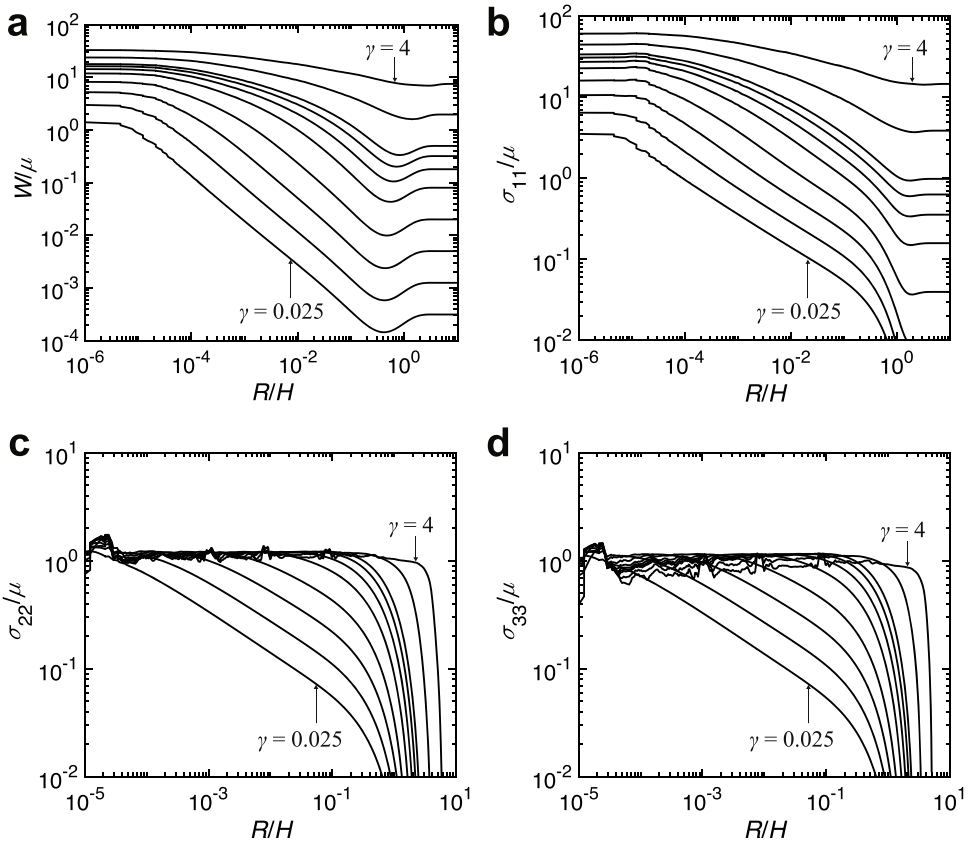

Fig. B1. Strain energy density and normal stress at $\Theta = 0$. (a) W/μ, (b) σ_{11}/μ, (c) σ_{22}/μ, and (d) σ_{33}/μ are plotted as functions of R/H for different applied strains γ.

constant coefficient. Note that the linear prediction in Eq. (7) is independent of the material behavior in the nonlinear elastic zone.

4.3. Corner toughness

The parameter k may be used to define the loading necessary to initiate fracture at the corner (Reedy and Guess, 1993, 1995; Dunn et al., 1997). Fracture initiates at the corner when k reaches a critical value, k_c, called the corner toughness. Using Eq. (5), we relate the corner toughness to the shear strength, τ_c, as

$$k_c = Y\tau_c H^m. \tag{8}$$

Next, we use Eq. (8) to calculate the corner toughness of the hydrogel (Fig. 10). Every data point in Fig. 3b corresponds to a corner toughness in Fig. 10. The corner toughness is independent of thickness and has an average value of 0.27 kPa $m^{0.41}$. Since the corner toughness is independent of the sample geometry, it is a material property.

Note that the maximum strain applied in our experiments was $\gamma = 2$ (Fig. 3). Therefore, we violate small-scale nonlinear elasticity when $\gamma > 0.8$. In calculating the corner toughness, we have assumed that small-scale nonlinear elasticity applies for all thicknesses. Although the simulation shows that small-scale nonlinear elasticity is only valid for $\gamma < 0.8$, our experimental data show that corner toughness is a material property up to $\gamma = 2$. For a tougher hydrogel that ruptures at larger strains, the non-singular field near the corner will have a more significant effect on the initiation of fracture. Characterizing fracture initiation near corners in highly stretchable hydrogels is the subject of an ongoing work.

We now estimate the nonlinear elastic zone size at the initiation of fracture using the corner toughness. Assume that nonlinear elasticity occurs when $\sigma_{12} \sim \mu$. Evaluating Eq. (4) at $\Theta = 0$, $R = R_N$, and $k = k_c$ yields

$$R_N \sim (k_c/\mu)^{1/m}. \tag{9}$$

This estimate does not reference the geometry of the sample or the material behavior in the nonlinear elastic zone. For our material, Eq. (9) gives $R_N \sim 60$ μm, which readily satisfies the condition for small-scale nonlinear elasticity: $R_N << R_L << H$. In the present work, the corner toughness is not high, enabling us to apply small-scale nonlinear elasticity for modest H.

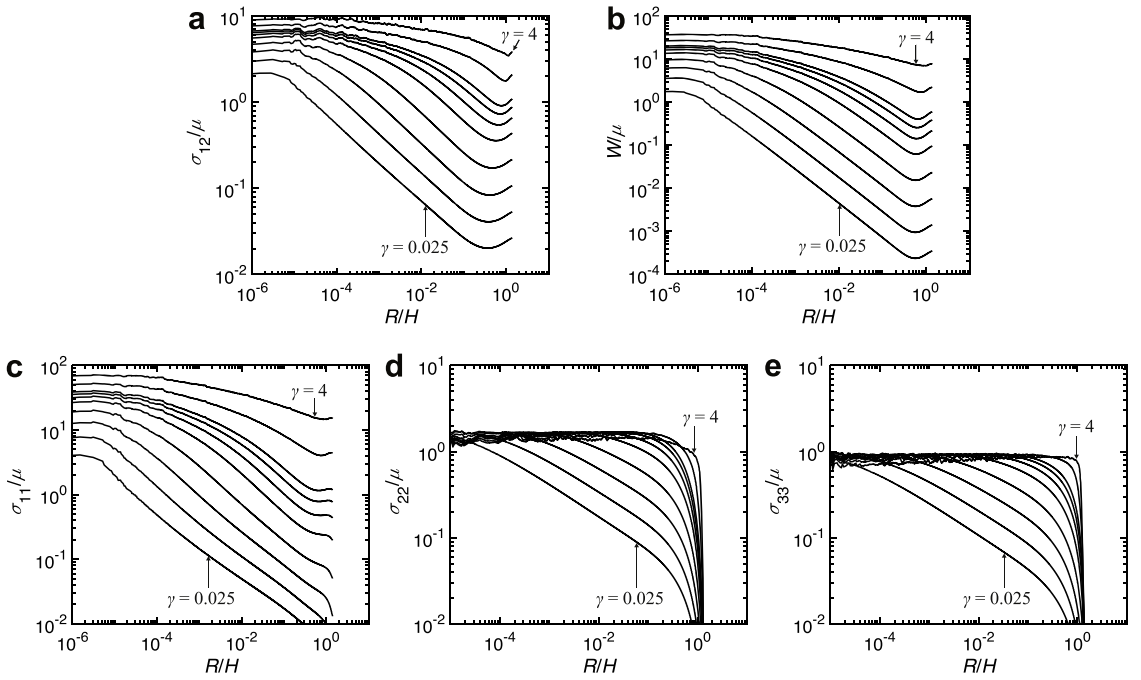

Fig. B2. Strain energy density and stress field at $\Theta = 45$ degrees. (a) σ_{12}/μ, (b) W/μ, (c) σ_{11}/μ, (d) σ_{22}/μ, and (e) σ_{33}/μ are plotted as functions of R/H for different applied strains γ.

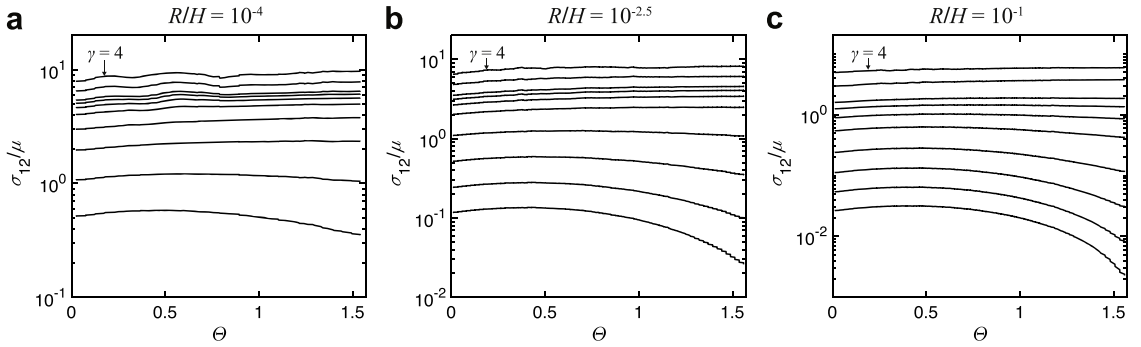

Fig. B3. Angular dependence of shear stress. σ_{12}/μ is plotted as a function of Θ for different applied strains γ. The distance from the corner is held constant at (a) $R/H = 10^{-4}$, (b) $R/H = 10^{-2.5}$, and (c) $R/H = 10^{-1}$.

5. Concluding remarks

We have studied the initiation of fracture from a corner in a hydrogel. We observe that the modulus is independent of thickness, but the strength scales with the thickness as $\sim H^{-0.4}$. This scaling is interpreted in terms of the elastic field around the corner. For a 90-degree corner and a neo-Hookean material, a finite element analysis shows a nonlinear elastic zone around the corner, in which the stress varies slowly. When the nonlinear elastic zone around the corner is much smaller than the thickness of the hydrogel, an annulus exists in which the linear elastic singularity prevails. Inside the annulus, the stress scales approximately as $\sim R^{-0.41}$. We show that such a condition of small-scale nonlinear elasticity applies even when the applied strain is as large as 80%. Consequently, the linear elastic singularity explains the experimentally observed scaling between strength and thickness. We calculate the corner toughness from the experimental data and show that it is a constant independent of thickness. This approach greatly simplifies the characterization of fracture initiated from corners of brittle soft materials.

CRediT authorship contribution statement

Jason Steck: Conceptualization, Methodology, Investigation, Formal analysis, Writing – original draft, Writing – review & editing. **Sammy Hassan:** Methodology, Software, Investigation, Formal analysis, Writing – original draft, Writing – review & editing. **Zhigang**

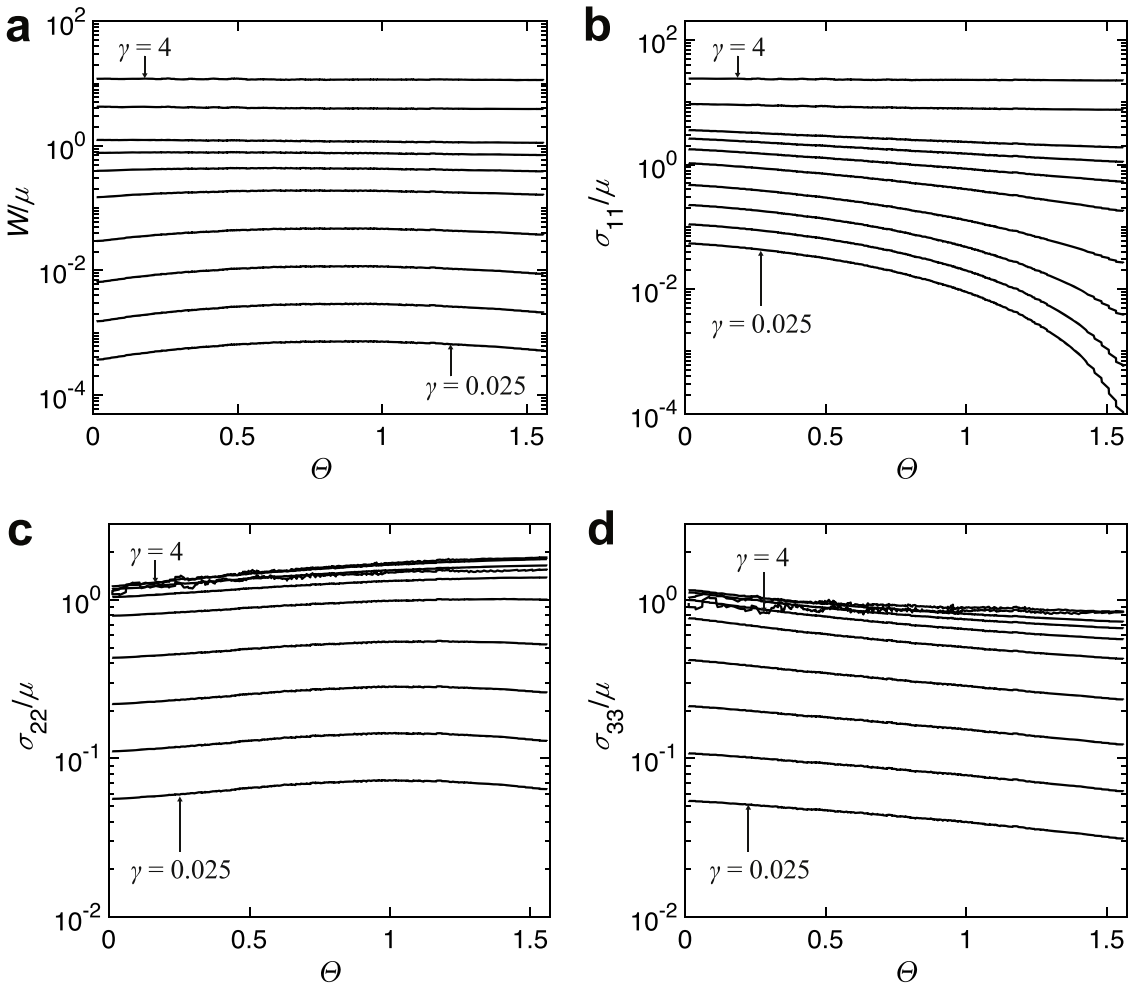

Fig. B4. Angular dependence of strain energy density and normal stress. (a) W/μ, (b) σ_{11}/μ, (c) σ_{22}/μ, and (d) σ_{33}/μ are plotted as functions of angle Θ for different applied strains γ. The distance from the corner is held constant at $R/H = 10^{-1}$.

Suo: Methodology, Funding acquisition, Supervision, Writing – review & editing.

Declaration of Competing Interest

The authors declare no conflict of interest.

Data Availability

Data will be made available on request.

Acknowledgment

This work was supported by MRSEC (DMR-2011754) and by the Air Force Office of Scientific Research (FA9550-20-1-0397). J.S. was supported by the NSF Graduate Research Fellowship (DGE1745303).

Statement of novelty

To the best of our knowledge, no existing work has a significant overlap with our submission.

Appendix A. Blatz-Ko wedge undergoing plane strain deformation on a rigid substrate

For a neo-Hookean material, the stress field near a corner under the plane strain conditions does not have a published analytical solution. There is a solution, however, to the stress field near an interface crack in a Blatz-Ko material undergoing plane strain deformation (Lengyel et al., 2014). Here we adapt their analysis to solve the nominal stress field for such a material near a wedge of angle Φ. We consider the incompressible limit, such that the Blatz-Ko material model reduces to neo-Hookean. We find that the nominal stress field is singular, and the singular exponent is $1 - \pi/2\Phi$. When $\Phi = 90$ degrees, $1 - \pi/2\Phi = 0$, and the asymptotic assumptions break down. Thus, the nominal stress field near the corner is not power-law singular. We also show that the true stress field near the corner is not power-law singular.

Consider a material particle denoted by $\boldsymbol{X}$ in the undeformed state and $\boldsymbol{x}$ in the deformed state (Fig. A1). A field of deformation of the body is described by the function $\boldsymbol{x}(\boldsymbol{X})$. A plane strain deformation requires that $x_3 = X_3$ for all $\boldsymbol{X}$. In the following, indices labeled with Greek letters can be either 1 or 2. The in-plane deformation gradient is $F_{\alpha\beta} = dx_\alpha/dX_\beta$, and has two scalar invariants: $I = F_{11}^2 + F_{12}^2 + F_{21}^2 + F_{22}^2$ and $J = F_{11}F_{22} - F_{12}F_{21}$.

Following Lengyel, we consider a compressible Blatz-Ko material model (Lengyel et al., 2014). Under the plane strain conditions, the Helmholtz free energy density W of this material is:

$$W = \frac{\mu}{2}(I-2) + \frac{\mu}{2\xi}\left(J^{-2\xi} - 1\right), \tag{A1}$$

where μ is the shear modulus and ξ is related to Poisson's ratio as $\xi = \nu/(1-2\nu)$. ξ represents the compressibility of the material. When the material is incompressible, $\nu = 0.5$, and ξ approaches infinity. In the following, we consider the limit as ξ approaches infinity.

The in-plane components of the nominal stress, $s_{\alpha\beta} = dW/dF_{\alpha\beta}$, are:

$$s_{\alpha\beta} = \mu F_{\alpha\beta} - \mu J^{-2\xi-1}\varepsilon_{\alpha\delta}\varepsilon_{\beta\omega}F_{\delta\omega} \tag{A2}$$

where $\varepsilon_{\alpha\beta}$ is the 2-dimensional Levi-Civita symbol.

In polar coordinates, static equilibrium in the absence of body forces, $ds_{\alpha\beta}/dX_\beta = 0$, gives:

$$\left(\frac{\partial^2}{\partial R^2} + \frac{1}{R}\frac{\partial}{\partial R} + \frac{1}{R^2}\frac{\partial^2}{\partial \Theta^2}\right)x_1 + (2\xi+1)J^{-2\xi-2}R^{-1}\left(\frac{\partial J}{\partial R}\frac{\partial x_2}{\partial \Theta} - \frac{\partial J}{\partial \Theta}\frac{\partial x_2}{\partial R}\right) = 0 \tag{A3a}$$

$$\left(\frac{\partial^2}{\partial R^2} + \frac{1}{R}\frac{\partial}{\partial R} + \frac{1}{R^2}\frac{\partial^2}{\partial \Theta^2}\right)x_2 - (2\xi+1)J^{-2\xi-2}R^{-1}\left(\frac{\partial J}{\partial R}\frac{\partial x_1}{\partial \Theta} - \frac{\partial J}{\partial \Theta}\frac{\partial x_1}{\partial R}\right) = 0, \tag{A3b}$$

where the polar coordinates (R, Θ) are defined in the undeformed state (Fig. A).

Assume the deformed coordinates x_1 and x_2 are separable and have the asymptotic form:

$$x_\alpha = R^n U_\alpha(\Theta), \tag{A4}$$

where n is a scalar between 0 and 1, and $U_\alpha(\Theta)$ are the angular functions. Taking the limits as $R \to 0$ and $\xi \to \infty$, the first terms of Eq. (A3) dominate. Thus, the governing equations reduce to $R^{n-2}(U_\alpha'' + n^2 U_\alpha) = 0$. Since the governing equations must hold for all R, they further reduce to a pair of linear, homogeneous 2nd order differential equations with constant coefficients:

$$U_\alpha'' + n^2 U_\alpha = 0. \tag{A5}$$

The governing equations constitute an eigenvalue problem for eigenfunctions U_α and eigenvalues n.

We set the boundary conditions such that the soft material is displacement-free at $\Theta = 0$ and traction-free at $\Theta = \Phi$. The displacement-free boundary condition requires that $x_1 = R$ and $x_2 = 0$ at $\Theta = 0$, while the traction-free boundary condition requires that $\frac{\partial x_\alpha}{\partial \Theta} = 0$ at $\Theta = \Phi$. In the limit as $R \to 0$, the boundary conditions are expressed in terms of U_α:

$$U_\alpha'(\Theta = \Phi) = 0 \tag{A6a}$$

$$U_\alpha(\Theta = 0) = 0 \tag{A6b}$$

The general solution to Eq. (A5) is $U_\alpha = a_\alpha \sin(n\Theta) + b_\alpha \cos(n\Theta)$, where a_α and b_α are constants. Applying the boundary conditions, the characteristic equation for n is $\cos(n\Phi) = 0$. The smallest positive integer solution gives:

$$n = \pi/2\Phi. \tag{A7}$$

The general solution becomes $U_\alpha = a_\alpha \sin(n\Theta)$, where a_α are constants related to the far field loading. The deformed coordinates are:

$$x_\alpha = a_\alpha R^{\pi/2\Phi} \sin\left(\frac{\pi\Theta}{2\Phi}\right) \tag{A8}$$

The in-plane components of the deformation gradient in polar coordinates are computed as $F_{\alpha\beta} = \frac{\partial x_\alpha}{\partial R}\frac{\partial R}{\partial X_\beta} + \frac{\partial x_\alpha}{\partial \Theta}\frac{\partial \Theta}{\partial X_\beta}$, giving:

$$F_{11} = a_1 n R^{n-1}(\sin n\Theta\cos\Theta - \cos n\Theta\sin\Theta)$$

$$F_{12} = a_1 n R^{n-1}(\sin n\Theta\sin\Theta + \cos n\Theta\cos\Theta)$$

$$F_{21} = a_2 n R^{n-1}(\sin n\Theta\cos\Theta - \cos n\Theta\sin\Theta)$$

$$F_{22} = a_2 n R^{n-1}(\sin n\Theta\sin\Theta + \cos n\Theta\cos\Theta) \tag{A9}$$

The deformation field in Eq. (A8) provides the weak estimate that $J = O(R^{2n-2})$. The asymptotic behavior of J is thus undetermined, and must depend on higher order terms of x_1 and x_2. However, this weak estimate does indicate that the leading order singular term of J is weaker than R^{2n-2}. We proceed without calculating the weaker order terms of J.

When J is singular, the first term of Eq. (A2) dominates as $R \to 0$ and $\xi \to \infty$. In this limit, the components of the nominal stress are:

$$s_{11} = \mu a_1 n R^{n-1}(\sin n\Theta\cos\Theta - \cos n\Theta\sin\Theta)$$

$$s_{12} = \mu a_1 n R^{n-1}(\sin n\Theta\sin\Theta + \cos n\Theta\cos\Theta)$$

$$s_{21} = \mu a_2 n R^{n-1}(\sin n\Theta\cos\Theta - \cos n\Theta\sin\Theta)$$

$$s_{22} = \mu a_2 n R^{n-1}(\sin n\Theta\sin\Theta + \cos n\Theta\cos\Theta) \tag{A10}$$

The singular exponent of the nominal stress field is $1 - n = 1 - \pi/2\Phi$. Perhaps surprisingly, Eqs. (A7), (A9), and (A10) are identical to those for a wedge of an incompressible neo-Hookean material under the plane stress conditions (Tarantino, 1999; Mo et al., 2021).

When $\Phi = \pi$, the problem reduces to an interface crack. In this case, $n = 1/2$ and all components of the nominal stress have a $R^{-1/2}$ singularity. As Φ decreases from π, the stress singularity weakens.

When $\Phi = \pi/2$, the problem reduces to a 90-degree corner. In this case, $n = 1$, and $F_{\alpha\beta}$, $s_{\alpha\beta}$, and J are not power-law singular. Moreover, the true stress, calculated as $\sigma_{\alpha\beta} = J^{-1}s_{\alpha\delta}F_{\beta\delta}$, is also not power-law singular. The true stress field may have a singularity weaker than that of a power-law, or it may be finite. This is in agreement with our finite element results inside the nonlinear elastic zone, where σ_{12} varies slowly over the resolution of our simulation, $R/H > 2 \times 10^{-6}$ (Fig. 6).

We note that when $\Phi = \pi/2$, the first terms of Eq. (A3) do not necessarily dominate as $R \to 0$. In this case, the governing equations may not be given by Eq. (A5). To proceed, we assume Eq. (A4) with $n = 1$, such that x_1 and x_2 are separable but $F_{\alpha\beta}$ is not singular. The governing equations become:

$$R^{-1}\left(U_1' + U_1\right) - R^{-1}(2\xi+1)\left(U_1U_2' - U_1'U_2\right)^{-2\xi-2}\left(U_1U_2' - U_1'U_2\right)U_2 = 0$$

$$R^{-1}\left(U_2' + U_2\right) + R^{-1}(2\xi+1)\left(U_1U_2' - U_1'U_2\right)^{-2\xi-2}\left(U_1U_2' - U_1'U_2\right)U_1 = 0. \tag{A11}$$

In the limit as $\xi \to \infty$, the second terms of Eq. (A11) dominate for all R. This is opposite to the conclusion when $n < 1$. Consequently, U_1 equals U_2 up to a constant coefficient. It is then required that $U_1U_2' - U_2U_1'$ and $U_1U_2'' - U_2U_1''$ are simultaneously zero. The second terms of Eq. (A11) equal zero for all R, and the governing equations again reduce to (A5), verifying our solution at $\Phi = \pi/2$.

Before we submitted this paper, a new paper was published online by H. Hui, B. Zhu, and M. Ciccotti, which solved the stress field near a wedge in a Blatz-Ko material undergoing plane strain deformation (Hui et al., 2022). Our results for the deformation and nominal stress are in agreement. In particular, the deformation gradient in Eq. (A9) matches their Eq. (50), and the nominal stress in Eq. (A10) matches their Eq. (51). However, their analysis is more complete than ours in two ways. First, they compute higher order terms in x_1 and x_2, providing the asymptotic behavior of J and $\sigma_{\alpha\beta}$. These higher order terms also contain effects of the compressibility parameter, ξ. Second, they find that when $\Phi = \pi/2$, the true stress field has a logarithmic singularity. The authors also note that there is no proof that the limit where $\xi \to \infty$ corresponds to a neo-Hookean incompressible solid.

Appendix B. Finite element results of stress field near the corner

For all figures in Appendix B, the stress field near the corner is evaluated at applied shear strains $\gamma = 0.025$, 0.05, 0.1, 0.2, 0.4, 0.6, 0.8, 1, 2, and 4. Each line in Figs. B1, B2, B3, and B4 correspond to one applied γ. All components of the stress field increase with γ, and can be identified by matching the order of the lines in each figure to the applied strains.

References

Anderson, T.L., 2017. Fracture Mechanics: Fundamentals and Applications, Fourth Edition, 4th. CRC Press, Boca Raton.

Banea, M.D., da Silva, L.F.M., 2009. Adhesively bonded joints in composite materials: an overview. Proc. Inst. Mech. Eng. Part J. Mater. Des. Appl. 223, 1–18. https://doi.org/10.1243/14644207JMDA219.

Bogy, D.B., 1971. Two edge-bonded elastic wedges of different materials and wedge angles under surface tractions. J. Appl. Mech. 38, 377–386. https://doi.org/10.1115/1.3408786.

Bouklas, N., Landis, C.M., Huang, R., 2015. Effect of solvent diffusion on crack-tip fields and driving force for fracture of hydrogels. J. Appl. Mech. 82, 081007 https://doi.org/10.1115/1.4030587.
Chai, H., 1986. A note on crack trajectory in an elastic strip bounded by rigid substrates. Int. J. Fract. 32, 211–213. https://doi.org/10.1007/BF00018354.
Chen, C., Wang, Z., Suo, Z., 2017. Flaw sensitivity of highly stretchable materials. Extreme Mech. Lett. 10, 50–57. https://doi.org/10.1016/j.eml.2016.10.002.
Cox, H.L., 1952. The elasticity and strength of paper and other fibrous materials. Br. J. Appl. Phys. 3, 72–79. https://doi.org/10.1088/0508-3443/3/3/302.
da Silva, L.F.M., das Neves, P.J.C., Adams, R.D., Spelt, J.K., 2009a. Analytical models of adhesively bonded joints—part i: literature survey. Int. J. Adhes. Adhes. 29, 319–330. https://doi.org/10.1016/j.ijadhadh.2008.06.005.
da Silva, L.F.M., das Neves, P.J.C., Adams, R.D., Wang, A., Spelt, J.K., 2009b. Analytical models of adhesively bonded joints—part II: comparative study. Int. J. Adhes. Adhes. 29, 331–341. https://doi.org/10.1016/j.ijadhadh.2008.06.007.
Dunn, M.L., Cunningham, S.J., Labossiere, P.E.W., 2000. Initiation toughness of silicon/glass anodic bonds. Acta Mater. 48, 735–744. https://doi.org/10.1016/S1359-6454(99)00352-3.
Dunn, M.L., Suwito, W., Cunningham, S., 1997. Fracture initiation at sharp notches: correlation using critical stress intensities. Int. J. Solids Struct. 34, 3873–3883. https://doi.org/10.1016/S0020-7683(96)00236-3.
Garyfallogiannis, K., Purohit, P.K., Bassani, J.L., 2022. Energy release rate for cracks in hydrogels undergoing finite deformations. J. Mech. Phys. Solids 167, 105009. https://doi.org/10.1016/j.jmps.2022.105009.
Hassan, S., Kim, J., Suo, Z., 2022. Polyacrylamide hydrogels. IV. Near-perfect elasticity and rate-dependent toughness. J. Mech. Phys. Solids 158, 104675. https://doi.org/10.1016/j.jmps.2021.104675.
Hein, V.L., Erdogan, F., 1971. Stress singularities in a two-material wedge. Int. J. Fract. Mech. 7 https://doi.org/10.1007/BF00184307.
Hong, W., Zhao, X., Zhou, J., Suo, Z., 2008. A theory of coupled diffusion and large deformation in polymeric gels. J. Mech. Phys. Solids 56, 1779–1793. https://doi.org/10.1016/j.jmps.2007.11.010.
Hui, C.-Y., Liu, Z., Minsky, H., Creton, C., Ciccotti, M., 2018. Mechanics of an adhesive tape in a zero degree peel test: effect of large deformation and material nonlinearity. Soft Matter 14, 9681–9692. https://doi.org/10.1039/C8SM01731J.
Hui, C.-Y., Zhu, B., Ciccotti, M., 2022. Finite deformation field near the tip of a Blatz–Ko wedge bonded to a rigid substrate. Int. J. Fract. https://doi.org/10.1007/s10704-022-00654-y.
Hutchinson, J.W., 1968. Singular behaviour at the end of a tensile crack in a hardening material. J. Mech. Phys. Solids 16, 13–31. https://doi.org/10.1016/0022-5096(68)90014-8.
Kim, J., Zhang, G., Shi, M., Suo, Z., 2021. Fracture, fatigue, and friction of polymers in which entanglements greatly outnumber cross-links. Science 374, 212–216. https://doi.org/10.1126/science.abg6320.
Labossiere, E.W., Dunn, P.L., 2001. Fracture initiation at three-dimensional bimaterial interface corners. J. Mech. Phys. Solids 49, 609–634. https://doi.org/10.1016/S0022-5096(00)00043-0.
Lengyel, T.H., Long, R., Schiavone, P., 2014. Effect of interfacial slippage on the near-tip fields of an interface crack between a soft elastomer and a rigid substrate. Proc. R. Soc. Math. Phys. Eng. Sci. 470, 20140497 https://doi.org/10.1098/rspa.2014.0497.
Liu, D., Fleck, N.A., 1999. Scale effects in the initiation of cracking in a scarf joint. Int. J. Fract. 95, 67–88. https://doi.org/10.1023/A:1018635914556.
Long, R., Hui, C.Y., 2015. Crack tip fields in soft elastic solids subjected to large quasi-static deformation — a review. Extreme Mech. Lett. 4, 131–155. https://doi.org/10.1016/j.eml.2015.06.002.
Long, R., Hui, C.-Y., Gong, J.P., Bouchbinder, E., 2021. The fracture of highly deformable soft materials: a tale of two length scales. Annu. Rev. Condens. Matter Phys. 12, 71–94. https://doi.org/10.1146/annurev-conmatphys-042020-023937.
Mo, C., Raney, J.R., Bassani, J.L., 2021. Finite deformation near a crack tip terminated at an interface between two neo-Hookean sheets. J. Mech. Phys. Solids 104653. https://doi.org/10.1016/j.jmps.2021.104653.
Noselli, G., Lucantonio, A., McMeeking, R.M., DeSimone, A., 2016. Poroelastic toughening in polymer gels: A theoretical and numerical study. J. Mech. Phys. Solids 94, 33–46. https://doi.org/10.1016/j.jmps.2016.04.017.
Reedy, E.D., 1990. Intensity of the stress singularity at the interface corner between a bonded elastic and rigid layer. Eng. Fract. Mech. 36, 575–583. https://doi.org/10.1016/0013-7944(90)90113-U.
Reedy, E.D., Guess, T.R., 1995. Butt joint tensile strength: interface corner stress intensity factor prediction. J. Adhes. Sci. Technol. 9, 237–251. https://doi.org/10.1163/156856195x01148.
Reedy, E.D., Guess, T.R., 1993. Comparison of butt tensile strength data with interface corner stress intensity factor prediction. Int. J. Solids Struct. 30, 2929–2936. https://doi.org/10.1016/0020-7683(93)90204-K.
Rice, J.R., Rosengren, G.F., 1968. Plane strain deformation near a crack tip in a power-law hardening material. J. Mech. Phys. Solids 16, 1–12. https://doi.org/10.1016/0022-5096(68)90013-6.
Tarantino, A.M., 1999. The singular wedge problem in the nonlinear elastostatic plane stress theory. Q. Appl. Math. 57, 433–451.
Truesdell, C., Noll, W., 2004. The Non-Linear Field Theories of Mechanics, 3. Springer Science & Business Media.
Wang, X., Hong, W., 2012. Delayed fracture in gels. Soft Matter 8, 8171. https://doi.org/10.1039/c2sm25553g.
Wang, Y., Yang, X., Nian, G., Suo, Z., 2020. Strength and toughness of adhesion of soft materials measured in lap shear. J. Mech. Phys. Solids 143, 103988. https://doi.org/10.1016/j.jmps.2020.103988.
Williams, M.L., 1952. Stress singularities resulting from various boundary conditions in angular corners of plates in extension. J. Appl. Mech. 19, 526–528.